Active rheology of phospholipid vesicles

Aidan T. Brown, Jurij Kotar, and Pietro Cicuta[*]

Cavendish Laboratory and Nanoscience Centre, University of Cambridge, Cambridge CB3 0HE, United Kingdom

Optical tweezers are used to manipulate the shape of artificial dioleoyl-phosphatidylcholine (DOPC) phospholipid vesicles of around 30 μm diameter. Using a time-shared trapping system, a complex of traps drives oscillations of the vesicle equator, with a sinusoidal time dependence and over a range of spatial and temporal frequencies. The mechanical response of the vesicle membrane as a function of the frequency and wavelength of the driving oscillation is monitored. A simple model of the vesicles as spherical elastic membranes immersed in a Newtonian fluid, driven by a harmonic trapping potential, describes the experimental data. The bending modulus of the membrane is recovered. The method has potential for future investigation of nonthermally driven systems, where comparison of active and passive rheology can help to distinguish nonthermal forces from equilibrium fluctuations.

PACS number(s): 87.16.D−, 87.80.Cc

I. INTRODUCTION

The equilibrium thermal fluctuations, called flickering, of phospholipid vesicle and erythrocyte membranes have been extremely well studied, both experimentally [1,2] and theoretically [3–5]. The dynamic aspects of these fluctuations are less well understood, owing to the large number of ways in which membrane fluctuations relax [6] and the fact that both microscopic observation [7] and scattering experiments [8] typically cannot probe the relaxation of pure dynamic eigenmodes. There has also been much recent interest in active or athermal membrane systems, particularly as applied to biology. Experiments have been performed on both model [9] and *in vitro* cellular [10] membrane systems to probe nonthermal membrane fluctuations, by looking at differences between the static and dynamic fluctuation spectra and the flickering predicted by the fluctuation dissipation theorem. In this paper, we describe experiments we have performed using optical tweezers to drive oscillations of giant vesicles, observing the membrane response and fitting this to a simple viscoelastic theory. The eventual aim is to apply this method of active membrane driving to simple biological systems, such as red blood cells, or to more complex model membranes containing protein pumps, where the active deformation should allow one to isolate thermal motion from nonthermal, active motion, in a similar spirit as was demonstrated on bulk systems in [11] and on living cells in [12].

II. METHODS

A. Production of giant unilamellar vesicles

Giant unilamellar vesicles (GUVs) are produced using the electroformation method first described by Angelova *et al.* [13]. Dioleoyl-phosphatidylcholine (DOPC) (Avanti Polar Lipids, Alabama), 3 mg/ml in chloroform, is deposited on the conducting side of an indium tin oxide (ITO) slide (VisionTek) and the lipid film is dried overnight under vacuum. A capacitive cell is formed with a second ITO slide with 0.5-mm-thick Teflon strips acting as spacers. The chamber is filled with

a sugar solution (100 mM sucrose, 2 mM sodium azide; Sigma Aldrich) and the ends sealed with vacuum grease and Parafilm. A 1 V peak to peak (p-p), 10 Hz sinusoidal signal is applied across the electroformation chamber for 2 h, then 1 V p-p, 2 Hz for 50 min. This produces GUVs, which are extracted and stored for up to two weeks at room temperature in the original sucrose solution. This protocol is based on an optimized method described in [14].

B. Imaging and manipulation of GUVs

Shortly before experiments are to be performed, GUVs in sucrose solution are resuspended in isotonic glucose solution at $50\times$ dilution. Optical adhesive (no. 61, Norland, New Jersey) is used to form a chamber of 125 μm thickness, between a cover slip and a microscope slide. 50 μl of GUV sample is injected using a micropipettor. After an evaporation period, described below, the ends of the chamber are sealed by optical adhesive and the adhesive cured under uv light. The refractive index difference between sucrose and glucose solutions allows the GUVs to be imaged easily under bright field illumination, and the density contrast causes the vesicles to settle at the base of the sample chamber, as described in [15]. Once the GUVs settle, the drift of their center of mass is neglible. GUVs are imaged at room temperature (22 °C) in a temperature controlled laboratory. They are found to have diameters between 10 and 80 μm, with the majority between 15 and 40 μm.

In order to give the best image quality, the focal plane is generally positioned 1–2 μm above the GUV equator, since on the equator itself the radial intensity profile across the contour varies around the equator, interfering with the flickering analysis described in Sec. III. Theoretical analysis (Sec. IV) assumes the GUV is imaged at its equator; in practice the focal plane offset is small compared to the GUV radius and is expected to have a neglible effect on the observed behavior.

Most GUVs are initially tense, or fluctuate only slightly. When an optical trap is applied to such GUVs, the thermal fluctuation amplitude drops dramatically, and they become too tense to be driven by oscillations of the trap. To solve this problem, the sample chamber is left unsealed for 90 min before use. Approximately 1/3 of the external glucose solution

evaporates, water moves out of the GUVs through osmotic pressure, and the GUVs acquire enough excess area to be deformed in the optical trap.

GUVs are illuminated in bright field with a halogen lamp and observed with an AVT Marlin F-131B complementary metal-oxide semiconductor camera, through a water immersion objective (Zeiss, Achroplan IR 63×, numerical aperture (NA) 0.9). The pixel size on screen is 93 nm, the recording frame rate is between 70 and 100 frames per second (fps) depending on GUV size, and the shutter time is ∼4ms.

C. Driving modes

The optical tweezers setup consists of a laser (IPG Photonics, PYL-1-1064-LP, $\lambda = 1064$ nm, $P_{max} = 1.1$ W) focused through the same objective as used for observation. The laser beam can be moved laterally in the focal plane via a pair of acousto-optic deflectors (AA Opto-Electronic, model AA.DTS.XY-250 at 1064 nm), controlled by custom built electronics allowing multiple trap generation with sub-nanometer resolution in the position of each trap, and switching between traps in a time of 50 μs. This permits the creation of complex time-shared traps consisting of up to 200 individual time-varying trap locations, as described in [16].

Optical forces have been used before to deform GUVs [17,18], and biological membranes [19]. Here, a complex of traps is defined, consisting of a ring of 24 uniformly spaced laser beams, leading to 24 discrete trapping positions that hold and deform GUV membranes. The focused optical traps produces a force on the membrane because of the asymmetry of the refractive index between the internal and external sugar solutions, as discussed in the Appendix. The total time for the laser to visit all 24 trap positions is of the order of 1 ms. This is much faster than the typical membrane relaxation time scales of ∼0.1–1 s, so that it is reasonable to approximate all the trap positions as being active continuously. Meanwhile, the shape of the complex trap is changed in 100 discrete steps per period, so again the time scale of these steps is much shorter than experimental time scales. However, it was initially found that the vesicle would drift out of the ring of traps during the experiment. It was deduced that this instability was caused by beating between the two short time scales: the laser switching time and the increment in trap shape. The instability vanished when the trap was moved diametrically between opposite points on the vesicle equator rather than progressively round the circle (Fig. 1). This star-shaped pattern was adopted for all experiments reported in this paper. Note that the work reported in Ref. [18] is close in spirit to the current investigation but the experiment is limited to the stress relaxation following vesicle extension.

The vesicle is first trapped in a static circular trap and allowed to equilibrate for ∼10 s and then driven by periodically changing the shape of the trap, with driving frequency ν. During each run of the experiment, which lasts approximately 7 min, the driving frequency is scanned over a range from 0.049 to 12.6 Hz, up and down in steps of factors of 2 (see Fig. 2). The amount of time and the number of periods spent on each frequency step was varied throughout the experiment, but was typically 4 periods per frequency, or 1 s, whichever was longer. No systematic difference in response was found
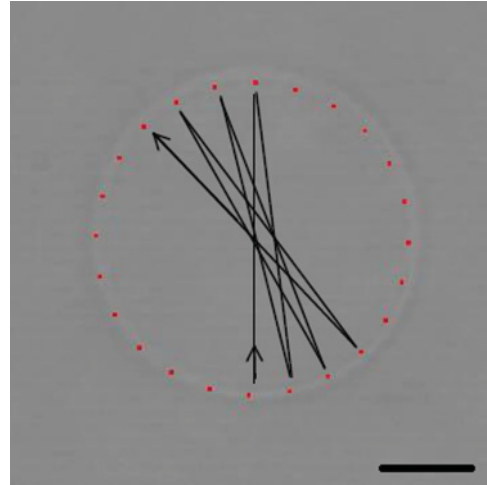
FIG. 1. (Color online) Bright field optical image shows a vesicle held in a ring of optical traps. The dots indicate the positions of 24 optical traps around the vesicle equator. In this image the traps define a circle; in the experiment traps are moved at a range of spatial and temporal frequencies. The arrows show the first few steps of the protocol for time sharing of the beam between trap positions. Scale bar is 5 μm.

between the parts of the experimental cycle where frequency was increasing or decreasing. In each video the complete cycle over ν is repeated two or three times. The evolution of the shape of the complex trap over time can be described as follows, ignoring the two short time steps. We give each trap a label i, running from 1 to 24 in a clockwise direction. For a particular frequency ν, the distance r_i of the trap i from the origin at the vesicle center, as a function of equatorial angle ϕ_i and time t, evolves as

$$r_i(\phi_i,t) = r_0 + \zeta_0 \cos(m\phi_i) \sin(\omega t), \tag{1}$$

where r_0 is the initial radius of the complex trap, which is chosen to be 1–2 μm smaller than the vesicle radius a. ζ_0 is the driving amplitude, typically 1 μm. The vesicle response to varying amplitude (from 0.25 to 2 μm) at fixed frequency was investigated separately, to test the linearity of the response. $\omega = 2\pi\nu$ is the angular frequency of the driving oscillation, and m is an integer mode number. Mode numbers of $m = 2$, 3, 4, and 6 are used. $m = 5$ is not used, in order that all modes have their maximum and minimum amplitudes at the position of a trap. Higher modes than $m = 6$ are not used, to avoid approaching the spatial Nyquist frequency at $m = 12$.

III. DATA ANALYSIS

Each frame is analyzed using a custom contour analysis programme in MATLAB (The Mathworks, Eugene, Oregon) to determine the radius of the vesicle equator r as a function of ϕ and t, as described in [7]. For each frame in the video, the center of the vesicle is first determined approximately. The contour is then split up into 360 equal angular segments. A radial intensity profile is extracted perpendicular to each angular segment. These radial profiles are combined by aligning their points of maximal gradient to create an average radial profile. Then each radial profile is correlated with the average profile. A
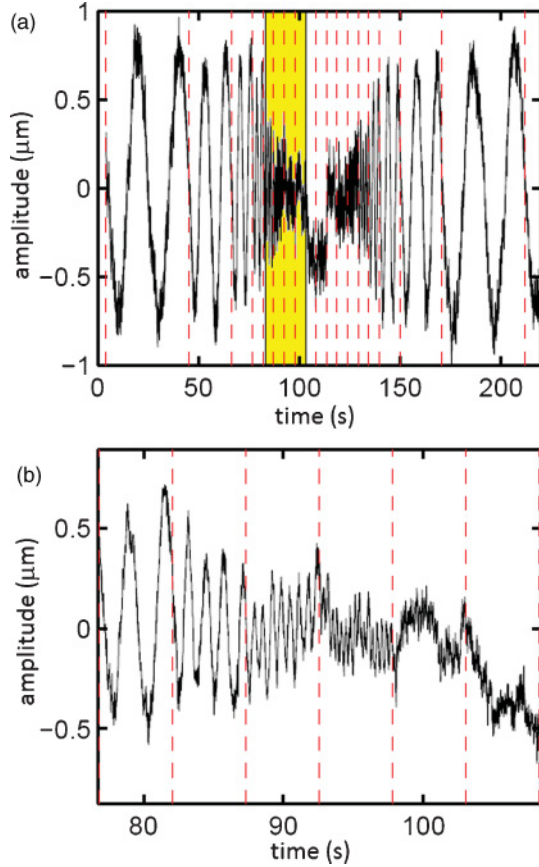
FIG. 2. (Color online) The vesicle can be deformed by moving optical traps. The panels show the membrane amplitude response traces for the second harmonic mode in one experiment, where the second harmonic mode itself is excited. (a) The full frequency scan in one experiment; the vertical dashed lines indicate the times at which the driving frequency is changed. (b) A closeup on the yellow (shaded) region in (a), to illustrate the higher frequencies. The sinusoidal response can be seen at both high and low frequencies, and the amplitude decreases with frequency. The amplitude and phase of the response, for various modes, are shown in Fig. 3.

parabola is fitted around the maximum in this filtered function. This gives a subpixel determination of the radial profile of each point, resulting in 360 equally spaced radial positions for each frame: the contour profiles. These contour profiles are spatially Fourier transformed, and the response of the excited spatial mode extracted. A typical response is shown in Fig. 2.

The amplitude of each spatial mode is found to have a random error of ± 10–30 nm, depending on image quality. This is comparable to the position resolution found in [20], where the same optical setup was used to track colloidal microspheres. The video is split up into sections, each corresponding to one temporal input frequency, and the temporal Fourier transform of each section is taken to give the phase and amplitude of the response at that excitation frequency. The driving oscillations of the complex trap are recorded separately, so that the relative phase of excitation and response can be determined to within one frame (~ 10 ms). The mean and the standard deviation in the mean of the response are taken from between four and six cycles over all frequencies in a single video.

IV. THEORY

A. Dynamics of Helfrich Hamiltonian

The relaxation time scales of thermal fluctuations on a spherical membrane have been derived in [3] and used to describe erythrocyte flicker in [10]. We extend this theory to sinusoidally driven oscillations. The Helfrich Hamiltonian F for an arbitrarily shaped membrane is given by

$$F = \int_S dS \left[2\kappa \left(H^2 - 2C_0 H + C_0^2 \right) + \sigma \right] - P \int_V dV, \quad (2)$$

where κ is the bending modulus coupling to the mean curvature H, and terms in the Gaussian curvature κ_G have been ignored, as these are topological invariants. The two Lagrange multipliers σ and P maintain respectively a constant total area S and volume V to second order in small fluctuations around the equilibrium shape. σ is the effective tension, and P is the pressure difference across the membrane. C_0 is the spontaneous curvature. In [3] Eq. (2) is expanded to second order around a background sphere of radius a, to give

$$\triangle F^{(2)} = \sum_{lm} \frac{U_{lm}^2}{2a^2} (l-1)(l+2)[a^2\sigma + l(l+1)\kappa], \quad (3)$$

where U_{lm} is the displacement, decomposed into the spherical harmonics Y_l^m, which are the eigenmodes of the Helfrich Hamiltonian on a spherical membrane. The spherical harmonics are defined as in [21] and normalized such that

$$\int_0^{2\pi} \int_0^{\pi} Y_l^m \left[Y_l^m \right]^* \sin\theta d\theta d\phi = 1. \quad (4)$$

In Eq. (3), we have neglected the spontaneous curvature, which is expected to vanish for a symmetrical membrane. While it is known that asymmetric internal and external solutions can also produce spontaneous curvature [22], we assume here that this effect is negligible since any direct interactions of the phospholipids with sucrose and glucose are likely to be very similar and so to cancel out. In general, a nonzero spontaneous curvature will have a significant effect on mode amplitudes, in that it modifies the equilibrium shape of the vesicle, as in [23], and hence the eigenmodes and eigenvalues of the equations of motion. However, the spontaneous curvature should have no direct effect on the stiffness of modes. This can be seen by making the replacement $\Delta H = H - C_0$ in Eq. (2). While the equilibrium curvature is modified, the effective bending stiffness is not.

Applying the equipartition function to Eq. (3) and projecting onto the equator as in [2] gives the mean squared displacement of each equatorial mode:

$$\frac{\langle |h_m|^2 \rangle}{a^2} = \sum_l \frac{b_{lm}^2 k_B T}{(l-1)(l+2)[a^2\sigma + l(l+1)\kappa]}, \quad (5)$$

where $b_{lm} = Y_l^m(\frac{\pi}{2}, 0)$, are the values of the spherical harmonics on the equator, and h_m is the Fourier transform of $h(\phi)$, the equatorial vesicle radius. For large l (equivalent to large q), Eq. (5) approaches the planar approximation used in [2,7] and other papers.

The equation of motion for each eigenmode is

$$f_{lm} = -4\pi \left[a\dot{U}_{lm} \eta Z(l) + \frac{\partial \Delta F}{\partial U_{lm}} \right], \quad (6)$$

where f_{lm} is the force acting on mode Y_l^m and where

$$Z(l) = \frac{(2l+3)(l-1)}{l} + \frac{(2l-1)(l+2)}{l+1}. \quad (7)$$

This is derived from the solution of Stokes equation in spherical harmonics in [24] and agrees with Peterson's calculations [Eq. (60) in [4]], neglecting membrane viscosity. However, Milner and Safran's calculation of $Z(l)$ differs from ours at low l [3], possibly due to differences in boundary conditions. By replacing f_{lm} with a random thermal force, and using the fluctuation dissipation theorem, one obtains the dynamics of thermal fluctuations, as in [3]. Consideration of the projection onto the vesicle equator gives an expression for the time correlation of equatorial fluctuations:

$$\langle h_m(t) h_m^*(t+\tau) \rangle_t = \sum_l b_{lm}^2 \langle |U_{lm}|^2 \rangle \exp\left(\frac{-\tau}{\tau_{lm}}\right), \quad (8)$$

where

$$\tau_{lm} = \frac{a^3 \eta Z(l)}{(l-1)(l+2)[a^2\sigma + l(l+1)\kappa]}. \quad (9)$$

This is the equivalent of the planar approximation Eq. (8) in [7] for spherical harmonics.

In the current work, the driving force for membrane motion is provided not by thermal fluctuations but by interactions between the membrane and a ring of optical traps. Here, we model the discrete ring of traps by a continuous ring whose displacement $\zeta_m(\phi)$ from the mean radius r_0 is specified by the continuous approximation of Eq. (1):

$$\zeta_m(\phi) = \zeta_0 \cos(m\phi) \sin(\omega t). \quad (10)$$

This continuous approximation is valid as long as the wavelength of the equatorial mode under consideration is longer than the intertrap spacing. The wavelength of the shortest mode studied ($m = 6$) is four times longer than the intertrap spacing. The force which the trap exerts on the membrane is derived by approximating each point in the complex trap as a Hookean spring, acting radially on the nearest equatorial point of the vesicle membrane. The validity of this approximation is addressed in the Appendix. The visible response $h(\phi,t)$ of the membrane equator is decomposed into equatorial and temporal harmonics as $h = h_m(\omega) \cos(m\phi) e^{i\omega t}$. Hence, the radial force f_{lm} produced by this ring of Hookean traps is

$$f_{lm} = 2\pi \beta b_{lm}(\zeta_m - h_m), \quad (11)$$

where ζ is the amplitude of the harmonic driving oscillation and β is the effective trapping stiffness, having units of N m^{-1}. An order of magnitude estimate of β is presented in the Appendix. We ignore thermal fluctuations because they are at random phase compared with the applied oscillations.

We note that the thermal fluctuations can produce a small renormalization of the bending modulus, to give an observed bending modulus κ_R of the form

$$\kappa_R = \kappa - \left(\frac{k_B T}{4\pi}\right) I \ln\left(\frac{q_{max}}{q_{min}}\right). \quad (12)$$

There has been much disagreement about the value and sign of the scaling constant I. Proposed values range from $I = -1$ in [5] to $I = 3$ in [25]. These differences stem from the use of two different measures, the mean curvature [5,26] or the normal displacement [25,27,28]. Monte Carlo simulations [29] have recovered a softening effect, consistent with $I > 0$, but it is not clear whether the simulations also suffer from the same dilemma over choice of measure. To calculate an order of magnitude estimate, we can take $I = 3$ and $q_{max}/q_{min} = 1000$ for definitiveness. This gives a maximum correction to κ of $\sim -2k_B T$. If, in the active experiments, as predicted for passive thermal flickering, the renormalization of κ does not depend on the time scale or wave number of the driving oscillations, then it will not modify the form of the membrane response. Furthermore, since the renormalization is caused by the thermal fluctuations, and since these fluctuations are present in both the active and passive experiments, we expect that any renormalization will occur to roughly the same extent in both cases, so that for the purposes of comparison the renormalization can be ignored.

We model the trap as continuous. This is valid in the spherical model, since, in the linear regime, there is no coupling between modes of different m. Combining Eqs. (3) and (11) and taking the Fourier transform gives

$$\frac{h_{0,m}}{\zeta_0} = \frac{\tilde{\beta} \sum_l b_{lm}^2 [i\tilde{\omega}Z(l) + \varsigma_l]^{-1}}{1 + \tilde{\beta} \sum_l b_{lm}^2 [i\tilde{\omega}Z(l) + \varsigma_l]^{-1}}, \quad (13)$$

where several dimensionless parameters are defined:

$$\varsigma_l = (l-1)(l+2)\tilde{\sigma} + (l-1)l(l+1)(l+2),$$

$$\tilde{\beta} = \frac{\beta a^2}{2\kappa}, \quad \tilde{\sigma} = \frac{\sigma a^2}{\kappa}, \quad \tilde{\omega} = \frac{\omega \eta a^3}{\kappa}.$$

It is useful to examine the limits of Eq. (13) at high and low frequency. At low frequency, the response is dominated by elastic contributions and reaches a plateau, set by a balance between the driving force β and the elastic resistance from κ and σ. At high frequencies, viscous damping becomes significant, and the response approaches the asymptotic limit:

$$\frac{h_{0,m}}{\zeta_0} = \frac{i\tilde{\beta} \ln(4\tilde{\omega}m^{-3})}{3\pi\tilde{\omega}}. \quad (14)$$

The logarithmic scaling in the high frequency limit comes from the l^4 dependence of the elastic terms in κ. These have a higher order l dependence than the competing viscous terms, so the viscosity is not able to completely dominate to give a pure l^{-1} decay. However, if the finite lateral extent of the trap is taken into account, this will lead to an effective cutoff in the summation over l at a mode l_{max} corresponding to the depth of focus of the trap, modifying the asymptotic decay to $\sim \omega^{-1}$. The same finite size effect is known to lead to modifications in the power spectra $P(\omega)$ of membrane motion from $P(\omega) \propto \omega^{-5/3}$ to $P(\omega) \propto \omega^{-2}$, when this motion is coupled to finite sized patches, for example, micrometer sized beads [30,31].

The dominant effect of the optical traps is not the dynamic motion produced by deforming the shape of the complex trap, but rather the static stretching produced by the traps in their mean position r_0. This produces two effects: an increase in tension, which can be seen from the reduced fluctuations of the vesicle when the trap is applied, and a change of shape. Without the effect of the trap, the vesicle has large amounts of excess area, so is far from spherical. When the trap is applied,

a certain amount of excess area is stretched out by the trap, and the mean radius of the vesicle typically increases by a few micrometers, giving an equilibrium membrane shape in the trap that is probably close to an oblate spheroid. The strictly spherical model above does not apply to arbitrarily shaped vesicles but the general principle remains similar, with the precise definition of some of the terms (b, α, ς) varying depending on the vesicle shape. We also expect the same high frequency behavior as in the spherical model, with a decay in amplitude scaling as $\ln(\omega)/\omega$, irrespective of the shape of the vesicle.

V. RESULTS

A. Active driving

In Fig. 3, the amplitude and phase of response are shown for a 30-μm-diameter vesicle. The solid lines are fits to Eq. (13), giving both the phase and amplitude of the vesicle response. The experimental response is transformed to give the effective vesicle modulus $h'_m = h_{0,m}/(\zeta_0 - h_{0,m})$, which has the advantage that its phase is independent of β. We fit the phase of h' for κ and σ and then fit the amplitude of h' for β, keeping other parameters fixed. This is found to be more robust than trying to fit all variable parameters at once. Fitting was performed using the *fminsearch* function in MATLAB. At 22 °C, the viscosities of 100 mM glucose and sucrose solutions are both within 5% of the viscosity of pure water [32], so the viscosity is set at the pure water value: $\eta = 10^{-3}$ Pa s. Solid curves are fits to theory for the parameters given in the figure caption. The mean fitted value of κ over 18 videos of 8 vesicles is $\kappa = (21 \pm 3)k_B T$.

There is generally good agreement between theoretical predictions and the experimental data, for both the phase and the amplitude of response, when σ and κ are allowed to vary freely. At high frequencies, however, the experimental amplitudes are consistently lower than theory predicts. There are several possible reasons for this. First, as shown in Fig. 2, when driven at high frequency, the trapping becomes unstable, that is to say, there is a systematic drift of the driven mode away from the undeformed position. This could be explained by the fact that at high frequencies the membrane does not follow the trap position closely. If the membrane in one part of the equator falls out of the linear trapping regime, then the driving is no longer stable. Another possible contribution comes from the finite size effect of the trap, as discussed in Sec. IV. This would lead to an ω^{-1} decay of the membrane response at high frequencies, indicated by the black line in Fig. 3(a).

In addition, the responses of the different harmonic modes as shown in Fig. 3 are not well described by a single trapping constant β. In Fig. 4, the fitted trapping constant is plotted as a function of the excited wave vector for eight vesicles. In general, the trapping strength decreases with increasing mode number. This is in line with the behavior of the predicted trapping force in the Appendix.

The linearity of the traps was tested by scanning over driving amplitudes, from 0.25 to 2 μm, at fixed frequency, at 0.2 and 1.6 Hz. This resulted in the plots shown in Fig. 5, which demonstrate that over the range of amplitudes studied, there is no significant nonlinear contribution from the driving amplitude.
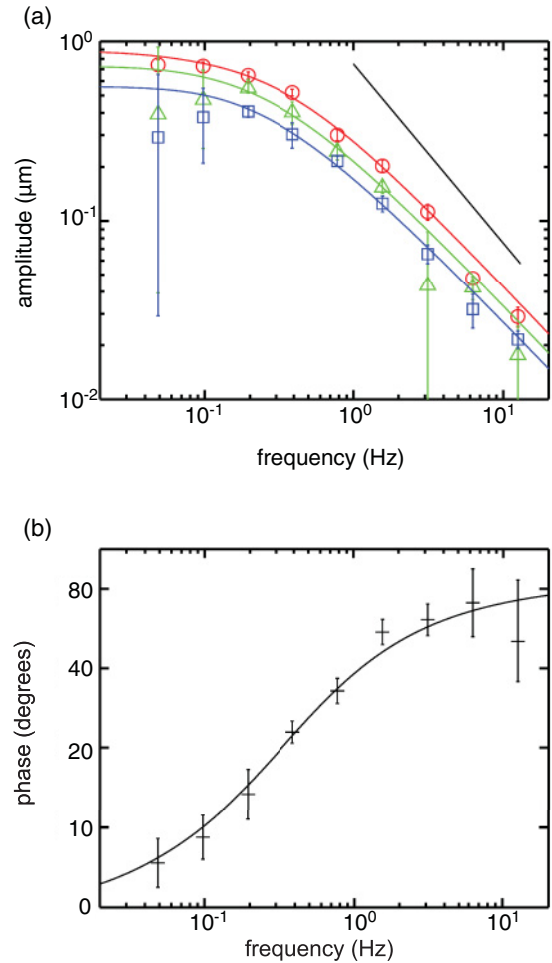
FIG. 3. (Color online) The vesicle response to applied optical force. (a) Membrane response amplitude of the harmonic modes 2 ($\bigcirc$), 3 ($\triangle$), and 4 ($\square$), when the respective modes are driven by optical traps, at $\zeta = 1$ μm, as a function of driving frequency. (b) The phase of response of the second harmonic mode of the same vesicle, corresponding to the second mode amplitude response above. The phase of the response to driving with modes 3 and 4 was not included because they overlap closely with the response of mode 2. The solid curves are lines of best fit of the theoretical response using Eq. (13), where first the parameters κ and σ are fitted to the phase (b) and then β is determined from the amplitude. Fitting gives $\sigma = 1.2 \times 10^{-8}$ N m^{-1}, $\kappa = 19k_B T$. The value of β varies with mode number as shown in Fig. 4. The black solid line in (a) represents the asymptotic ω^{-1} decay discussed in the text.

B. Flickering analysis

The thermal flickering of the vesicle can be monitored simultaneously with the active deformation. The effect of the driven oscillations on the flickering amplitudes can be clearly seen: Driving a particular mode increases the observed mean squared static fluctuation of that mode, as expected, typically without any effect on nearby modes, as is evident in Fig. 6. In the presence of a membrane tension, which is here caused by the optical trapping of the vesicle, a measure of the bending modulus κ requires access to particularly high mode numbers. Unfortunately, the video quality was on the whole too low to
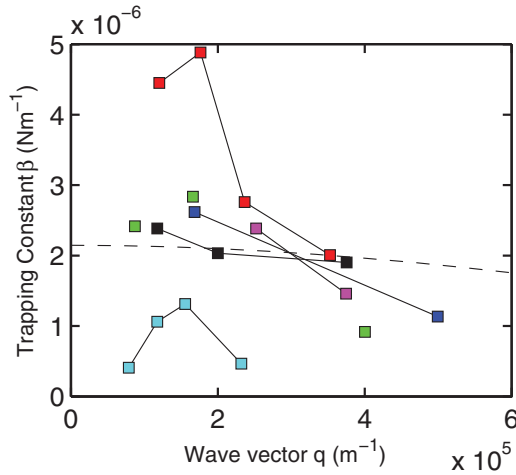
FIG. 4. (Color online) The values of trapping constant β, extracted by fitting experimental data for all vesicles considered in this study. β is plotted versus the wave number q of the driving oscillation. Colored connected markers correspond to data from a single vesicle. The unconnected green markers represent vesicles for which only one data point was obtained. Most vesicles show a decay of β with increasing wave number. The dashed line is a theoretical estimate of β obtained from Eq. (A12), for a 30-μm-diameter vesicle and other parameters as specified in the Appendix.

reliably determine the high mode number parts of the contour, with a sufficient precision for the accurate determination of κ. While this needs to be kept in mind in future experiments, it is a limit that is readily addressed by using a higher quality camera and a higher NA objective. The driven modes themselves could be accurately determined because they are all long wavelength modes, and because they are at a known frequency.

In parallel with the current experiments, we examined DOPC GUVs produced using the same protocol as in Sec. II,
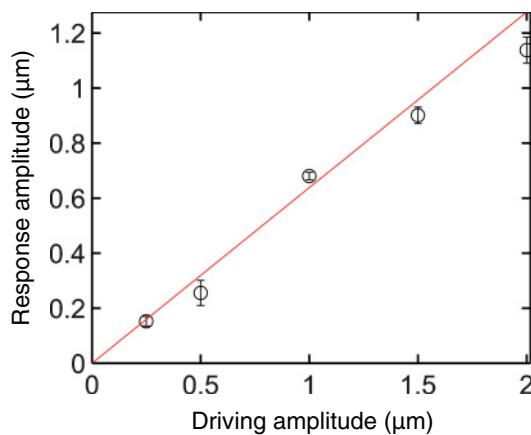
FIG. 5. (Color online) The response is linear: data in this figure are for mode 2, with varying driving amplitude, at a constant frequency of 0.2 Hz. The error bars are the standard deviation in the mean over multiple oscillations for a single vesicle. The order in which the amplitudes were investigated was randomized. The solid line is a line of best fit passing through the origin, demonstrating the linearity of the response. Similar linearity was seen for driving at 1.6 Hz and at both frequencies with a second vesicle.
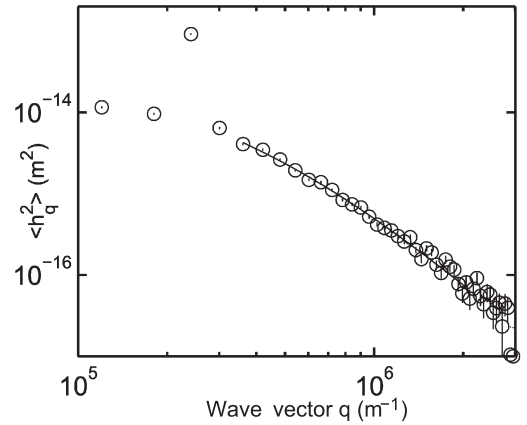
FIG. 6. The flickering spectrum for a vesicle, obtained while driving the fourth harmonic mode. In spite of the driven oscillations the static spectrum is largely unaffected, except for the fourth mode itself (clearly visible here as the highest $\langle h_q^2 \rangle$ value). The solid line is a fit to the planar static spectrum, giving $\kappa = 14 k_B T$. At low wave vectors the fluctuation spectrum is dominated by tension, as apparent from the weak wave vector dependence.

using traditional flickering methods, and the contour analysis method discussed in [7], and obtained a mean bending modulus of $\kappa = (27.3 \pm 3.2) k_B T$ over a sample of 60 vesicles, which is consistent with the value obtained from actively driving the deformations.

C. Flickering dynamics

We also extract the time correlation function for the lowest modes, up to $m = 12$: Fig. 7. As shown in [7] and in Sec. IV the time correlation function should be an infinite sum over exponentials, given by Eq. (9), rather than a single exponential. This is because the nonequatorial modes of the vesicle, which contribute to the observed equatorial spectrum of fluctuations, also decay, and each of these modes has its own time scale. At long times, the correlation function approaches a single exponential decay corresponding to the lowest energy equatorial mode. At short times, all modes contribute, and at intermediate times there is a rapid crossover to the long time behavior as these higher energy modes decay away.

However, it was found empirically that at short time differences ($t < 0.1$ s), the time correlation functions in Fig. 7 were fitted better by a single exponential with an effective time constant τ' than by the sum over many exponentials in Eq. (9). This could be explained by the fact that the calculation of the correlation function Eq. (9) depends strongly upon the assumption that the vesicle is quasispherical. There will also be perturbing effects on the dynamics from the proximity to the cover slip. No attempt was made to fit the correlations at longer times, since the nonexponential form of the long time correlations varies widely between experimental videos and is probably caused by the limitations in the contour fitting which are described in Sec. V B.

We follow the same method of analysis as in [7]: a single exponential is fitted to the theoretical correlation functions over a wide range of material parameters, resulting in an effective theoretical decay time scale τ'. This effective time scale is found to be well fitted by a simple power law of τ_0 alone,
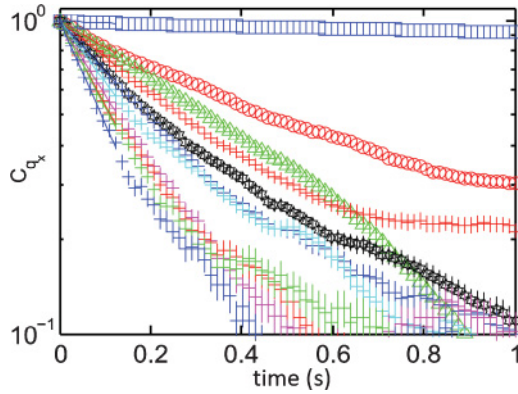
FIG. 7. (Color online) At short times, equatorial modes decay with a well defined time scale. The normalized correlation functions C_q for modes 2–12 of the 30 μm vesicle in Fig. 3 are plotted here. Markers correspond to mode numbers: 2 ($\bigcirc$), 3 ($\triangle$), 4 ($\square$), 6 ($\star$). Other modes are represented by crosses. In these data, the fourth mode is excited, and as expected it displays a much slower decay compared to the other modes. Solid lines are fits of single exponentials $\exp{(-t/\tau')}$ to the first ten delay times, and results for τ' are plotted in Fig. 8.

FIG. 8. (Color online) Time scale of decay τ' for several videos taken with the same vesicle. ($\bigcirc$) driving mode 2; ($\triangle$) driving mode 3; ($\square$) driving mode 4; (+) vesicle in static trap; ($\times$) vesicle without trap. The mode corresponding to the driven mode has a long time correlation; other modes are unaffected by the driving to within uncertainty. The solid and dashed lines are respectively the q^{-1} and q^{-3} limits discussed in the text. Coloured lines connect points, to guide the eye.

where τ_0 is the theoretical long time decay constant corresponding to the equatorial mode. The empirically determined function τ' (applicable for $\eta = 10^{-3}$ Pa s, $10^{-12} < \sigma < 10^{-7}$ N m^{-1}, $2k_BT < \kappa < 200k_BT$, $10^5 < q < 1.5 \times 10^6$ m^{-1}, $0.01 < \tau_0 < 100$ s) is $\tau' = 0.57\tau_0^{0.88}$. This effective time scale is determined for delay times of between one and eight frames, where noise has not yet become significant; see Fig. 7. Within the range defined above, the effective theoretical time scale is within 20% of this empirical function. This apparent power-law scaling between τ_0 and τ' is not universal, and only applies to the intermediate range of delay times where most of the high q modes have decayed away, but where the decay has not yet become entirely dominated by the longest relaxation time.

We then fit a single exponential to the corresponding experimental data and use the empirically determined relation between τ' and τ_0 to estimate the experimental decay time of the longest mode. This approximate method should be strictly valid only for a quasispherical vesicle. However, it should still give a more accurate estimate than simply assuming that the time correlation function corresponds to the decay of the equatorial mode alone.

The results of this fitting are shown in Fig. 8 for several videos recorded from a single vesicle. Between modes 5 and 12, the decay time scales are well fitted by a $\tau_0 \sim q^{-1}$ decay, as would be expected for tension dominated fluctuations [see Eq. (9)]. The vesicles which were driven showed a much longer correlation time in the mode that was driven than in other modes, as shown in Figs. 7 and 8.

VI. CONCLUSIONS

With a simple quasispherical model, we obtain a quantitative prediction of the phase and amplitude of vesicle response to driving with a ring of optical traps around the vesicle equator. However, because of the relatively poor bright field video quality, it was not possible to obtain a simultaneous

estimate of the bending modulus from the thermal flickering. Also, in the conditions studied here, the active method is not superior to the thermal flickering in terms of sensitivity to the bending modulus, since only long wavelength harmonic modes are excited, and these are dominated by the effective tension. Nevertheless, the mean value of $\kappa = (21 \pm 8)k_BT$ obtained from fitting the response to driving is consistent with typical values of κ for DOPC vesicles in the literature [for example, $(23.1 \pm 3.5)k_BT$ in [33]], and with values of κ obtained from thermal flickering studies in our laboratory. The power of this active deformation approach will be to enable studies of more complex systems, such as, for example, multicomponent vesicles, vesicle membranes coupled to membrane proteins, and red blood cells. By actively driving these systems over a wide range of length and time scales, it should be possible to characterize behavior which is not apparent from passive observation of equilibrium thermal fluctuations.

APPENDIX: TRAPPING FORCE

This appendix contains calculations of the force exerted on the equator of a vesicle by a ring of optical traps. The calculation assumes a spherical vesicle and a Gaussian beam focused at the vesicle equator. The calculation uses an energy density approach, rather than geometric optics, because it is simpler to take account of a Gaussian beam in the energy density approach. However, the energy density method is not rigorously correct, because it does not take account of the scattered radiation as geometric optics does. Nevertheless, the energy density approach and geometric optics were found to give similar solutions for the force on the equator, differing

only in a prefactor of order unity. Thus, only the energy density approach is included here.

The optical trap is approximated as a Gaussian beam, traveling along the z axis and focused on the origin. The beam has a time averaged mean squared electrical field $\langle E^2 \rangle$ given in cylindrical polar coordinates (ρ, ϕ, z) by [34]

$$\langle E^2(t, \rho, z) \rangle = \frac{A_0^2}{1 + \left(\frac{z}{z_d}\right)^2} \exp\left[-\frac{2\rho^2}{d^2\left(1 + \left(\frac{z}{z_d}\right)^2\right)}\right],$$
(A1)

where A_0 is a constant. A_0 can be related to the total beam power P by using the definition of the power as an integral over any surface A perpendicular to the light path [34]:

$$P = \frac{c\epsilon_0}{2\pi} \int_A dA \langle E^2 \rangle.$$
(A2)

For simplicity we take A to be the focal plane, $z = 0$. Performing the integral gives

$$A_0^2 = \frac{4P}{c\epsilon_0 d^2},$$
(A3)

and therefore

$$\langle E^2(t, \rho, z) \rangle = \frac{P}{c\epsilon_0 \sigma_\rho(z)^2} \exp\left[-\frac{\rho^2}{2\sigma_\rho(z)^2}\right],$$
(A4)

where

$$\sigma_\rho = \sqrt{\frac{d^2\left(1 + \left(\frac{z}{z_d}\right)^2\right)}{4}}.$$
(A5)

In a diffraction limited beam, the width of the beam in the focal plane ($d/2$) is similar to the wavelength of light, so in the current case $d \sim 2\ \mu$m.

Now, suppose the space to be separated into two volumes V_1 and V_2 with relative permittivities ϵ_1 and ϵ_2. The energy density difference W between the beams passing through V_1 and V_2 will be given by

$$W = \frac{\epsilon_0 \Delta\epsilon \langle E^2 \rangle}{4},$$
(A6)

where $\Delta\epsilon = \epsilon_2 - \epsilon_1$ is the difference in relative permittivity between the two volumes. Suppose a membrane of negligible thickness separates the two volumes. The normal pressure p of the optical field on this membrane is equal to the energy density W at that point. For the case of the Gaussian beam described above, p is given by

$$p = \frac{P\Delta\epsilon}{4c\sigma_\rho(z)^2} \exp\left[-\frac{\rho^2}{2\sigma_\rho(z)^2}\right].$$
(A7)

For fluid volumes, the only stresses in the system will occur on the membrane. In reality, the membrane also refracts the trapping beam, producing stresses on the membrane away from the equator, but these are not included in this order of magnitude estimate.

The pressure field of more complex traps is a linear supposition of the pressure field of the component pointlike traps. In particular, for a continuous ring of optical traps in

the plane $z = 0$, with variable radius $r(\phi)$, the pressure field is given by

$$p = \frac{P\Delta\epsilon}{8\pi c\sigma_\rho^2} \int_0^{2\pi} d\alpha$$
$$\times \exp\left(-\frac{\rho^2 + r(\alpha)^2 - 2\rho r(\alpha)\cos(\alpha - \phi)}{2\sigma_\rho^2}\right),$$
(A8)

where α is a dummy angle.

The spring constant of the complex traps used in the current paper can be found approximately by setting $r = r_0 + \zeta \sin(m\phi)$ and $z = 0$, and taking the derivative of Eq. (A8) with respect to ζ around $\zeta = 0$. This gives

$$\frac{\partial p}{\partial \zeta} \approx -B \int_0^{2\pi} d\gamma \exp\left(\frac{4\rho r_0 \cos(\gamma)}{d^2}\right)$$
$$\times \cos(m\gamma)[r_0 - \rho\cos(\gamma)],$$
(A9)

where

$$B = \frac{P\Delta\epsilon \sin(m\phi)}{\pi cd^4} \exp\left(-\frac{2(\rho^2 + r_0^2)}{d^2}\right),$$
(A10)

and where $\gamma = \alpha - \phi$ is another dummy angle. The value of β, the spring constant of the optical trap, can be found by integrating the pressure over the vesicle and factoring out the dependence on the trap position. For a small vertical focal distance z_d, β is given approximately by multiplying Eq. (A9) by z_d:

$$\beta = \frac{2\pi a p_{eq} z_d}{\sin(m\phi)},$$
(A11)

which gives

$$\beta \approx -\frac{8az_d P\Delta\epsilon}{cd^4} \exp\left(-\frac{2(a^2 + r_0^2)}{d^2}\right)$$
$$\times \int_0^{2\pi} d\gamma \exp\left(\frac{4ar_0\cos(\gamma)}{d^2}\right) \cos(m\gamma)[r_0 - a\cos(\gamma)].$$
(A12)

Hence, the trapping constant β depends in a nontrivial way on the mode number m which is excited. However, in the limit of pointlike traps, the mode dependence vanishes, since $d/\sqrt{ra}$ approaches zero, and the integral in Eq. (A12) is dominated by the Gaussian decay. If we also assume $a \sim r$ and define $\delta = r - a$, this gives

$$\beta \approx -\frac{4\sqrt{2\pi}\delta z_d P\Delta\epsilon}{cd^3} \exp\left(-2\frac{\delta^2}{d^2}\right),$$
(A13)

where $\delta = r_0 - a$ is the difference between the radius of the trap and the membrane. In order to have a finite trapping stiffness, δ and d must be of similar order, also implying $a \sim r$. This is also the case experimentally: typically the mean trap radius traps lies approximately 1 μm inside the vesicle equator. If $r_0 > a$, then Eq. (A13) suggests that the force on the membrane will lie in the opposite direction to the motion of the traps. This is formally correct, but this situation is unstable toward rigid translation of the membrane. In this limit, Eq. (A13) can be used to give an order of magnitude estimate of β. The refractive index of sugar solutions can be obtained

from [35], which gives $\Delta\epsilon \sim 9 \times 10^{-3}$ for an internal solution of 100 mM sucrose and an external solution of 100 mM. The total trapping power P is approximately 100 mW. The small length scales d, δ, and z_d are all of order 2 μm. For a 30-μm-diameter vesicle, this gives $\beta \sim 2 \times 10^{-6}$ N m^{-1}, which is similar to the experimentally determined values of

β shown in Fig. 4. It is hard to make more than an order of magnitude estimate of β, since, according to Eq. (A13), β should scale very strongly with the length scales δ and d. For nonpointlike traps, with larger trapping width d, the trapping will tend to decrease with increasing mode number m. This is also demonstrated experimentally in Fig. 4.

---

[1] F. Brochard and J. F. Lennon, J. Phys. (France) **36**, 1035 (1975).

[2] J. Pecreaux, H. G. Dobereiner, J. Prost, J. F. Joanny, and P. Bassereau, Eur. Phys. J. E **13**, 277 (2007).

[3] S. T. Milner and S. A. Safran, Phys. Rev. A **36**, 4371 (1987).

[4] M. A. Peterson, Mol. Cryst. Liq. Cryst. **127**, 257 (1985).

[5] H. A. Pinnow and W. Helfrich, Eur. Phys. J. E **3**, 149 (2000).

[6] M. Kraus and U. Seifert, J. Phys. (France) **4**, 1117 (1994).

[7] Y.-Z. Yoon, H. Hong, A. Brown, D. C. Kim, D. J. Kang, V. L. Lew, and P. Cicuta, Biophys. J. **97**, 1606 (2009).

[8] A. G. Zilman and R. Granek, Phys. Rev. Lett. **77**, 4788 (1996).

[9] P. Girard, J. Prost, and P. Bassereau, Phys. Rev. Lett. **94**, 088102 (2005).

[10] T. Betz, M. Lenz, J.-F. Joanny, and C. Sykes, Proc. Natl. Acad. Sci., USA **106**, 15312 (2009).

[11] M. Atakhorrami, J. I. Sulkowska, K. M. Addas, G. H. Koenderink, J. X. Tang, A. J. Levine, F. C. MacKintosh, and C. F. Schmidt, Phys. Rev. E **73**, 061501 (2006).

[12] D. Mizuno, R. Bacabac, C. Tardin, D. Head, and C. F. Schmidt, Phys. Rev. Lett. **102**, 168102 (2009).

[13] M. I. Angelova, S. Soleau, P. Meleard, J. F. Faucon, and P. Bothorel, Prog. Colloid Polym. Sci. **89**, 127 (1992).

[14] S. L. Veatch and S. L. Keller, Phys. Rev. Lett. **89**, 268101 (2002).

[15] R. Dimova, A. Said, N. Bezlyepkina, V. Nikolov, K. A. Riske, and R. Lipowsky, J. Phys.: Condens. Matter. **18**, 1151 (2006).

[16] M. Leoni, J. Kotar, B. Bassetti, P. Cicuta, and M. Cosentino Lagomarsino, Soft Matter **5**, 472 (2009).

[17] C. Poole and W. Losert, in *Methods in Molecular Biology 400: Methods in Membrane Lipids*, edited by A. M. Dopico (Humana Press, Totowa, NJ, 2007), pp. 389–404.

[18] H. Zhou, B. B. Gabilondo, W. Losert, and W. van de Water, Phys. Rev. E **83**, 011905 (2011).

[19] J. Guck, R. Ananthakrishnan, and H. Mahmood, Biophys. J. **81**, 767 (2001).

[20] G. M. Cicuta, J. Kotar, A. T. Brown, J.-H. Noh, and P. Cicuta, Phys. Rev. E **81**, 051403 (2010).

[21] K. Riley, M. Hobson, and S. Bence, *Mathematical Methods for Physics and Engineering*, 2nd ed. (Cambridge University Press, Cambridge, UK, 2004)

[22] P. G. Petrov, J. B. Lee, and H.-G. Döbereiner, Europhys. Lett. **48**, 435 (1999).

[23] H.-G. Dobereiner, G. Gompper, C. K. Haluska, D. M. Kroll, P. G. Petrov, and K. A. Riske, Phys. Rev. Lett. **91**, 048301 (2003).

[24] J. Happel and H. Brenner, *Low Reynolds Number Hydrodynamics* (Martinus Nijhoff, The Hague, 1983)

[25] L. Peliti and S. Leibler, Phys. Rev. Lett. **54**, 1690 (1985).

[26] W. Helfrich, J. Phys. (France) **46**, 1263 (1985).

[27] D. Forster, Phys. Lett. **114A**, 115 (1986).

[28] H. Kleinert, Phys. Lett. A **114**, 263 (1986).

[29] G. Gompper and D. M. Kroll, J. Phys. I (France) **6**, 1305 (1996).

[30] A. J. Levine and F. C. MacKintosh, Phys. Rev. E **66**, 061606 (2002).

[31] Y.-Z. Yoon, J. Kotar, A. T. Brown, and P. Cicuta, Soft Matter **7**, 2042 (2011).

[32] P. Nikam, H. Ansari, and M. Hasan, J. Mol. Liq. **87**, 97 (2000).

[33] N. Fa, L. Lins, P. Courtoy, Y. Dufrêne, P. V. D. Smissen, R. Brasseur, D. Tyteca, and M.-P. Mingeot-Leclercq, Biochim. Biophys. Acta—Biomembranes **1768**, 1830 (2007).

[34] S. A. Akhmanov and S. Y. Nikitin, *Physical Optics* (Clarendon Press, Oxford, 1997)

[35] W. M. bin Mat Yunus and A. bin Abdul Rahman, Appl. Opt. **104**, 3341 (1988).